MNRAS **000**, 1–11 (2018) Preprint 1 October 2018 Compiled using MNRAS LATEX style file v3.0

Optical properties of the Resonant Drag Instabilities (RDIs)

U. P. Steinwandel[1,2⋆] Alexander Kaurov[3] and Philip F. Hopkins[4]
[1]*Universitäts-Sternwarte München, Fakultät für Physik, LMU Munich, Scheinerstr. 1, D-81679, Germany*
[2]*Max Planck Institut für Astrophysik, Karl-Schwarzschild-Str. 1, D-85741 Garching, Germany*
[3]*Institute for Advanced Study, 1 Einstein Drive, Princeton, NJ 08540, USA*
[4]*TAPIR, Mailcode 350-17, California Institute of Technology, Pasadena, CA 91125, USA*

Accepted XXX. Received YYY; in original form ZZZ

ABSTRACT
In recent studies (Squire & Hopkins 2018b) a new general super class of dust-gas-mixture instabilities is reported called the resonant drag instabilities (RDIs). These instabilities have been studied recently in more detail in a series of papers (Hopkins & Squire 2017, 2018; Squire & Hopkins 2018a) to understand the growth rate of the instabilities in the linear regime. In this study we start to investigate the general optical properties that are caused by the appearance of the RDIs. Therefore, we perform idealized simulations which utilize a reduced system of units depending only on the grain sizes, the dust-to-gas ratio and the dust drift velocity. We investigate the grain size distributions along different line of sights and calculate the geometrical optical depth in the boxes. This leads to the understanding that the geometrical optical depth in the box is fixed by the initial conditions and only depends on the assumed grain size distribution. The RDIs could be interesting in many applications in astrophysics whenever dust plays a major role. Due to the universality of the applied unit system it is possible to make constraints for various astrophysical systems. One of the most interesting astrophysical systems where the RDIs could be important is in AGB-star winds which are believed to be driven by radiation pressure on dust in the Atmosphere (Höfner & Olofsson 2018).

Key words: Keywords: instabilities — turbulence — ISM: kinematics and dynamics — star formation: general — galaxies: formation — stars: AGB and post-AGB — planets and satellites: formation

1 INTRODUCTION

Dust is a very important ingredient of various astrophysical phenomena covering a wide range of scales. In star formation dust is a crucial coolant which makes the collapse of protostars possible once they exceed the stage of pure isothermal collapse. Once the medium in the collapsing gas cloud becomes optically thick, dust makes it possible to radiate energy away in the infrared regime, which leads to the further collapse of the cloud and finally the formation of a star. In planet formation dust appears in protoplanetary discs and plays a major role in both favored models of planet formation the core accretion model and the disc instability model. Further, dust is important in the field of astrochemestry where it is e.g. important as a catalyst for the formation of molecular hydrogen. Moreover, dust can influence the detailed heating and cooling properties of the ISM within galaxies and can strongly influence the feedback process of active galactic nuclei (AGN). Furthermore, the winds of AGB stars can be explained by an interplay of pulsation-induced shock waves and the radiation pressure on the dust (e.g. Höfner & Olofsson 2018).
In a recent series of papers Hopkins & Squire (2017, 2018); Squire & Hopkins (2018b,a) it has been pointed out that there is a super-class of instabilities when dust particles move through gas. These instabilities build up when the phase velocity of the gas phase is matching the drift velocity of the dust particles. Therefore, these instabilities are called resonant drag instabilities (RDIs). The growth rates of this instabilities are maximized at a certain resonant wave number, resulting in a certain resonant angle.

In this study we focus on the the acoustic modes of the RDIs which are triggered by neutral dust particles moving through a box with a fluid of neutral charge and a homogeneous gas density distribution. Further, in this simulations the dust particles are accelerated with a constant driving force. While Hopkins & Squire (2017) studied the linear regime of the acoustic modes in great detail, Moseley et al. in prep focus on the non linear regime of the acoustic modes to understand the behavior of the RDIs in that regime. This report is structured as follows. In chapter 2 we will discuss in more detailed how the fluid is coupled to the dust particles, explain briefly the numerical methods that we use to solve the equations of hydrodynamics and how the dust is coupled to it and explain how we constrain the Initial Conditions (ICs) to set up this problem. In chapter 3 we will calculate the optical depth of the dust-gas-mixture boxes and show that this is a constant throughout the simulations that

⋆ E-mail: usteinw@usm.lmu.de

© 2018 The Authors

only depends on the underlying grain size-distribution. In chapter 4 we start the discussion of our results by presenting the morphology of the instabilities, the grain size distribution in the instabilities as well as the calculation of the optical depth along different line of sights (LOS). Finally, in chapter 5 we present the the unit system that we constrain to the boxes under the assumption of typical values for AGB-star winds.

2 NUMERICAL METHODS AND SIMULATIONS

In this section we briefly discuss the numerical methods that are needed to model the RDIs in certain regions of interest. For this cause we partially use the simulations that are carried out by Hopkins & Squire (2018) and run new simulations with different dust to gas ratios but include the same physics to investigate a lareger sample of the parameter space. The simulations are carried out in a dimensionless unit system. This rises the opportunity to apply the simulations to several astrophysical regions of interest where dust is believed to have a major impact on the underlying physics. We imagine that the RDIs appear in the atmosphere of an AGB-star which winds are mainly driven by dust (Höfner & Olofsson 2018). All these simulations include a grain size spectrum following Mathis et al. (1977).

2.1 System of equations

We present the systems of equation that is taken into account within our simulations. In general there are three parts that we need to consider to treat the system properly. The first is the equation of motion (EOM) of the dust. The second is the EOM of the gas (Eulers-equation). The third is the coupling of the dust with the gas (and vice versa). For the dust grains the EOM can be directly integrated for each individual dust grain by solving

$$\frac{d\mathbf{v}_\mathrm{d}}{dt} = -\frac{\mathbf{w}_\mathrm{s}}{t_\mathrm{s}} + \mathbf{a}, \tag{1}$$

in co-moving coordinates with the constant external acceleration $\mathbf{a}$ on the dust grain, the drift velocity $\mathbf{w}_\mathrm{d} = \mathbf{v}_\mathrm{d} - \mathbf{u}_\mathrm{g}$, which is given as the relative movement between dust ($\mathbf{v}_\mathrm{d}$) and gas particles $\mathbf{u}_\mathrm{gas}$ and the stopping time t_s. In our simulations the stopping time is given under the assumption of Epstein-drag which leads to the following expression in both sub- and super-sonic regimes following (Draine & Salpeter 1979)

$$t_\mathrm{s} = \sqrt{\frac{\pi\gamma}{8}}\frac{\rho_\mathrm{d} a_\mathrm{d}}{\rho_\mathrm{g} c_\mathrm{s}}\left(1 + \frac{9\pi\gamma}{128}\frac{\mathbf{w}_\mathrm{d}^2}{c_\mathrm{s}^2}\right)^{-1/2}, \tag{2}$$

with the gas density ρ_g, the adiabatic index γ of the gas given by $\partial \log P_\mathrm{g}/\rho_\mathrm{g}$ with the pressure P_g within the fluid, the grain density ρ_d, the grain size-radius a_d and the sound speed $c_\mathrm{s} = \sqrt{\partial P_\mathrm{g}/\partial\rho_\mathrm{g}}$. The gas component is modeled via Eulers-equation, including a term that models the coupling (drag-force) of the dust on the gas particles.

$$\rho_\mathrm{g}\left(\frac{\partial}{\partial t} + \mathbf{u}_\mathrm{g}\cdot\nabla\right)\mathbf{u}_\mathrm{g} = -\nabla P_\mathrm{g} + \int d^3 v_\mathrm{d} f_\mathrm{d}(\mathbf{v}_\mathrm{d})\frac{\mathbf{w}_\mathrm{s}}{t_\mathrm{s}}. \tag{3}$$

The last term on the right hand-side of equation 3 is the coupling term for the drag force that the gas particles feel in the presence of the dust. The function $f_\mathrm{d}(\mathbf{v}_\mathrm{d})$ is the given phase-space density of the underlying distribution of the dust particles, where the grain density is given by evaluating the expression $\rho_\mathrm{d} = \int d^3 v_\mathrm{d} f_\mathrm{d}(\mathbf{v}_\mathrm{d})$. While in the recent studies of (Hopkins & Squire 2017; Squire & Hopkins 2018a) and Moseley et al. in prep the focus was on studies of the growth rate in the linear regime (Hopkins & Squire 2017; Squire & Hopkins 2018a) or the non-linear regime (Moseley et al. in prep.) respectively it is convenient to treat the grain size parameter as a constant to get a clearer answer on the underlying growth rates of the RDIs in the system. However, in our studies we apply a grain size distribution of the form

$$\frac{dN}{da} \propto a_\mathrm{d}^{-3.5}, \tag{4}$$

with the grain size a_d, following the grain size distribution from the interstellar dust model of Mathis et al. (1977). This dust model is constructed by taking the extinction of star light into account that passes through the sight lines of diffuse clouds (e.g. Weingartner & Draine 2001). Including a grain size spectrum of the form that is presented in equation 4 gives us the opportunity to study the influence of different grain sizes on the geometrical optical depth.

2.2 Numerical Methods

The simulations are carried out with the multi-method code Gizmo (Hopkins 2015). The equations of hydrodynamics are solved with the second-order Lagrangian Godunov finite volume method, the mesh less finite volume (MFV). The method has been well tested over the past few years (e.g. Gaburov & Nitadori 2011; Hopkins 2015) and shows a significant improvement over state of the art SPH-implementations (e.g. Hu et al. 2014; Beck et al. 2016) in terms of capturing shocks and solving fluid-mixing instabilities. The method shares similarities with both, SPH-methods and grid-based methods for solving the equations of hydrodynamics. While the density field is calculated in a SPH-like manner by evaluating the weighted sum over the neighboring particles, the equations for the fluxes are solved over the one-dimensional Riemann-problem on the surface between those particles up to second order precision, with an appropriate second order estimate for the gradients as well. Therefore, the Lagrangian nature of the method makes it by definition very close to state of the art moving-mesh methods (e.g. Springel 2010) with a different partition of the volume.
The dust particles in the simulations are modeled using the super particle approach (e.g. Carballido et al. 2008; Johansen et al. 2009; Bai & Stone 2010; Pan et al. 2011). The EOM of each super-particle obeys equation 1.

2.3 Initial Conditions and units

Hopkins & Squire (2017) showed the existence of an equilibrium solution with a constant dust- to-gas ratio $\mu = \langle\rho_\mathrm{d}\rangle/\langle\rho_\mathrm{g}\rangle$, the gas velocity $\langle\mathbf{u_g}\rangle = \langle\mathbf{u}_0\rangle + \mathbf{a}t\mu/(1+\mu)$ and the dust drift $\langle\mathbf{w}_\mathrm{s}\rangle = \mathbf{a}\langle t_\mathrm{s}\rangle/(1+\mu)$. The parameter $\mathbf{u}_0$ determines the velocity of the fluid for $t = 0$ and $\mathbf{a}$ specifies the acceleration (e.g. acceleration due to radiation pressure). Further, the system is specified by the stopping time given by $\langle t_\mathrm{s}\rangle = t_\mathrm{s}(\langle\rho_g\rangle\mathbf{w}_\mathrm{s})$. The simulations are initialized by assuming this equilibrium solutions at $t = 0$ fully periodic 3D Box with the box length $L0$ with $\langle\mathbf{u}_0\rangle = 0$ and $\langle\mathbf{w}_\mathrm{s}\rangle = \mathbf{a}\langle t_\mathrm{s}\rangle/(1+\mu)$. While Moseley et al. in prep focus on resolution studies of these systems to study the non linear growth regime of the RDIs using constant grain sizes we want to investigate a more specific case. We investigate the system in a regime when the grains have variable

sizes following the grain size distribution given by equation 4 The simulations are carried out with 256^3 gas particles and $4 \cdot 256^3$ dust particles for the two different cases. In the first case we assume that the dust particles feel the same acceleration regardless of their size. In the second configuration we assume the more realistic/physical case of dust particles which feel an acceleration depending on their grain size. The particles are initialized on a uniform grid. This leads to very good results and seems to perform very well compared to other methods for initializing the particle positions (e.g. using a glass-distribution) as shown in Moseley et al. in prep.
The setup is initialized in the most general way that is possible. We work in dimensionless units in terms of the equilibrium sound speed $\langle c_s \rangle$ and gas density $\langle \rho_g \rangle$ and the box size L_0. In this context, the system has only three free parameters, the dust-to-gas ratio μ, the acceleration of the dust particles $\mathbf{a}L_0/\langle c_s^2 \rangle$ and the grain size parameter α given by $\rho_d a_d / \langle \rho_g L_0 \rangle$. The choice of dimensionless units is motivated by two aspects. The first one is to focus on the detailed structure of the RDI. The second one is to keep the system as general as possible. Potentially there are a lot of regions within the universe where this instabilities can have a huge impact on the dynamics, like in giant molecular clouds (GMCs), winds of AGB-stars or the surrounding medium of AGN. The systems for which we can work out a more detailed framework in physical coordinates will be presented in chapter 5.

3 CALCULATING THE OPTICAL DEPTH

In this section we discuss the calculation of the optical depths for constant grain size and varying grain size given by the Mathis et al. (1977) grain size distribution.

3.1 Constant grain sizes

For constant grain sizes we can calculate the optical depth for the box analytically from the initial setup that has been used in the simulations. In the case of constant grain sizes our system is characterized by the grain size parameter which takes the form

$$\frac{a_d \rho_d}{L_{Box} \rho_g} = \text{const.} = 0.15, \tag{5}$$

with a_d as the grain size, ρ_d as the mean grain density, L_{Box} as the box size and ρ_g as the mean gas density in the box. For this system we can calculate the optical depth τ_{opt} of the box by:

$$\tau_{opt} = \sigma_d N_d, \tag{6}$$

with the cross-section of the dust particles σ_d and the column density of the dust N_d within the box. Further, we make the assumption of perfectly spherical grains (which is a very simplified assumption). Therefore, the cross section of the dust particles σ_d is given by the projected surface area of one dust particle.

$$\sigma_d = \pi a_d^2. \tag{7}$$

The column density of the dust grains in the box can be calculated via

$$N_d = \frac{\Sigma_d}{m_d}, \tag{8}$$

where Σ_d is the surface density of the dust particles in the Box and m_d is the mass of one dust particle. Σ_d can be calculated straightforward with the dust-to-gas ratio $\mu = 0.01$ and, the box size L_{Box} and the gas density ρ_{gas} in the box. Thus, the $\Sigma_d = \mu L_{Box} \rho_{gas}$. For spherical dust particles the mass of one dust particle is $m_d = \frac{4}{3}\pi a_d^3 \rho_d$. Thus the column density N_d is given by

$$N_d = \frac{\mu L_{Box} \rho_g}{\frac{4}{3}\pi a_d^3 \rho_d}. \tag{9}$$

We obtain the optical depth of the system if we use 7 and equation 9 and plug them into equation 6. This leads to the following result.

$$\tau_{opt} = \frac{3}{4}\mu \frac{L_{Box}\rho_g}{\rho_d a_d} = \frac{3}{4}\frac{\mu}{\alpha}. \tag{10}$$

By using equation 5 in equation 10 we obtain the optical depth $\tau_{opt} = 0.05$. From equation 10 one can immediately see that the optical depth of the box is only dependent on the initial configuration of the grain size parameter alpha and the dust to gas ratio μ.
Moreover, one can calculate τ_{opt} numerically by summing over all dust particles in the box and taking into account that we use the super particle approach for the dust particles where each dust particle in the simulation represents a statistical ensemble of dust particles. Thus, we have to re normalize with the particle mass. We obtain τ_{opt} by

$$\tau_{opt} = \frac{3}{4}\mu \frac{\sum_i a_{i,d}^2}{\sum_i m_i} \frac{m_d}{\frac{4}{3}a_d^3} = 0.05. \tag{11}$$

This is just a simple sanity check to make sure that we obtain the same values for τ_{opt} analytically and numerically. Moreover, we note that the optical depth for constant grain sizes is given by the initial value we choose in equation 5. If we keep this value fixed while transforming the unit less system into a physical system we keep the optical depth of the system fixed.

3.2 Variable grain sizes

Obtaining the optical depth in the case of variable grain sizes is more complicated but we will point out that the result is a re normalized version of equation 10 . In this case the optical depth can be calculated from the dust opacity κ_d.

$$\tau_{opt} = \int \kappa_d \rho_g dl. \tag{12}$$

This means we can calculate τ_{opt} by averaging κ_d and ρ_g over the total box size L_{Box}. This implies for τ_{opt}

$$\tau_{opt} = \overline{\kappa}_d \overline{\rho}_g L_{Box} \tag{13}$$

To evaluate $\overline{\kappa}$ we need to take the distribution of the grains into account. The grains are distributed following the power law given by equation 4 We can use equation 4 to get $\overline{\kappa}_{dust}$ introduced in equation 13.

$$\overline{\kappa}_d = \frac{\int \pi a_d^2 \frac{dN_d}{da} da}{\frac{1}{\mu}\int \frac{4}{3}\pi a_d^3 \overline{\rho}_d \frac{dN_d}{da} da}, \tag{14}$$

again we calculate the particle mass by assuming that the dust

particles are perfect spheres. We can then obtain a similar form as in equation 10 re scaled by the factor $\widetilde{a}$ with

$$\widetilde{a}_{\mathrm{d}} = \frac{\int a_{\mathrm{d}}^3 \frac{dN_{\mathrm{d}}}{da}}{\int a_{\mathrm{d}}^2 \frac{dN_{\mathrm{d}}}{da}} \tag{15}$$

By inserting $\widetilde{a}_{\mathrm{grain}}$ of equation 15 into equation 14 we find for the optical depth τ_{opt}

$$\tau_{\mathrm{opt}} = \frac{3}{4}\mu \frac{L_{\mathrm{Box}} \overline{\rho}_{\mathrm{gas}}}{\overline{\rho}_{\mathrm{d}} \widetilde{a}_{\mathrm{grain}}}. \tag{16}$$

However, $\widetilde{a}_{\mathrm{grain}}$ can directly be calculated from the grain distribution by inserting equation 4 in equation 15 and integrating the expression between a_{min} and a_{max}. Therefore, one obtains

$$\widetilde{a}_{\mathrm{grain}} = \frac{\int_{a_{\mathrm{min}}}^{a_{\mathrm{max}}} a^{-\frac{1}{2}} da}{\int_{a_{\mathrm{min}}}^{a_{\mathrm{max}}} a^{-\frac{-3}{2}} da} \approx \sqrt{a_{\mathrm{min}} a_{\mathrm{max}}}. \tag{17}$$

If we insert all the numbers we obtain an optical depth which is one order of magnitude larger than in the case of constant grain sizes. Thus $\tau_{\mathrm{opt}} = 0.5$.
Further, we can do the same calculation numerically by evaluating the expression

$$\tau_{\mathrm{opt}} = \mu \frac{\sum_i a_{\mathrm{i,grain}}^2 \frac{m_i}{\frac{4}{3} a_{\mathrm{i,grain}}^3}}{\sum_i m_i}. \tag{18}$$

By evaluating this expression over the total box we obtain $\tau_{\mathrm{opt}} = 0.5$.
From this calculations we can see that the optical depth within the boxes is a fundamental constant when we switch to a physical reference frame, because it is just a physical re scaling of the reduced unit system that has been applied in the simulations to study various modes of the RDIs. For both cases we adopt some similar unit conversions regarding the grain sizes and the mean grain density.

4 RESULTS

In this chapter we present our results. We start with a short discussion of the morphology of the instabilities in section 4.1 followed by a discussion of the grain size distributions along different line of sights through the box in section 4.2 and a discussion of the properties of the geometrical optical depths throughout the boxes in section 4.3.

4.1 Morphology of the instabilities

We start our discussion of the results by visualizing the results we obtain from the two simulations on which we base our studies on the general optical properties that arise in the presence of the RDIs. We introduce the shortcuts *RDI-const* and *RDI-noconst* for the two simulations based on the fact that in the model *RDI-const* the acceleration that the particles feel is independent of the grain size, while in the model *RDI-noconst* we present the more realistic case of a grain size dependent acceleration, as we pointed out in section 2.3. In figure 1 we show a time sequence of the model *RDI-const* for four different points in time. In figure 2 we show the time evolution of the model *RDI-noconst* for the same points in time. Although, both simulations start from the exact same initial conditions the build up of the RDIs is completely different between both simulations. In the case of the model *RDI-const* we can observe that the RDIs build up in sheets which are moving through the box, before they build up elongated cylinders through the whole box. The initial behaviour of the movement of the dust in the model 1 can be explained by the fact that all dust particles are initialized with the same acceleration within the simulation domain. Therefore, the dust particles move initially with the exact same velocity and their movement is strongly coupled. Once the RDIs build up and begin to dominate the system we see different structures like isolated islands of dust or elongated cylinders. As one can see from the comparison with the model *RDI-noconst* which we present in 2 the morphology of the RDIs is heavily influenced by a grain sized dependent acceleration. The initial build up is also dominated by sheets but other structures for more quickly and in a much more random fashion compared to the model *RDI-const*. Further, we note that the build up of the instabilities is more rapidly in the model in the model *RDI-noconst* than in the model *RDI-const*.

4.2 Grain size distribution and correlation of dust and gas

Apart from the morphology it is interesting to take a closer look to the distribution of the grain sizes within certain line of sights. In figure 3 we show the mean over 100 histograms along different line of sights for two different points in time ($t = 5$ and $t = 15$) for the models *RDI-const* (top) and *RDI-noconst* (bottom). This reveals that the RDIs are dominated by the large grains if we apply the same driving force for all particles. However, this behaviour turns around if we use a grain size dependent acceleration. In this case the scatter of the relation indicates that the RDIs are dominated by the smallest grain sizes. Further, we want to investigate how strongly the dust is coupled to the gas as a function of time. Therefore, we introduce a bias in analogy to cosmology (Kaiser 1984). The bias is introduced in cosmology to define the correlation between dark matter and galaxy population we can define a bias between the gas and the dust population within the simulation. In general one cane define a bias for almost everything by considering an over density of the following form.

$$b = \frac{\delta_{\mathrm{g}}}{\delta_{\mathrm{d}}}, \tag{19}$$

with $\delta_{\mathrm{gas}} = (\rho_{\mathrm{gas}} - \langle \rho_{\mathrm{gas}} \rangle)/\langle \rho_{\mathrm{gas}} \rangle$ as the gas over density and $\delta_{\mathrm{gas}} = (\rho_{\mathrm{dust}} - \langle \rho_{\mathrm{dust}} \rangle)/\langle \rho_{\mathrm{dust}} \rangle$ as the dust over density. We can calculate the bias by calculating the surface density of both, gas and dust particles along a certain line of sight on a grid. We use a grid with a resolution of 256x256. We show our results in figure 4. The top panel shows the time evolution of the bias while the middle and the bottom panel show the dust over density as a function of the gas over density for two different points in time ($t = 5$, middle and $t = 15$, bottom). The bias increases over time which indicates that the correlation between dust and gas becomes stronger with time. This argument is strengthened by taking the phase space of the dust and gas over densities into account (middle and bottom panel). While for early times there is nearly no correlation one can see for later times that the phase space is dominated by dust over densities due to the build up of the RDIs.

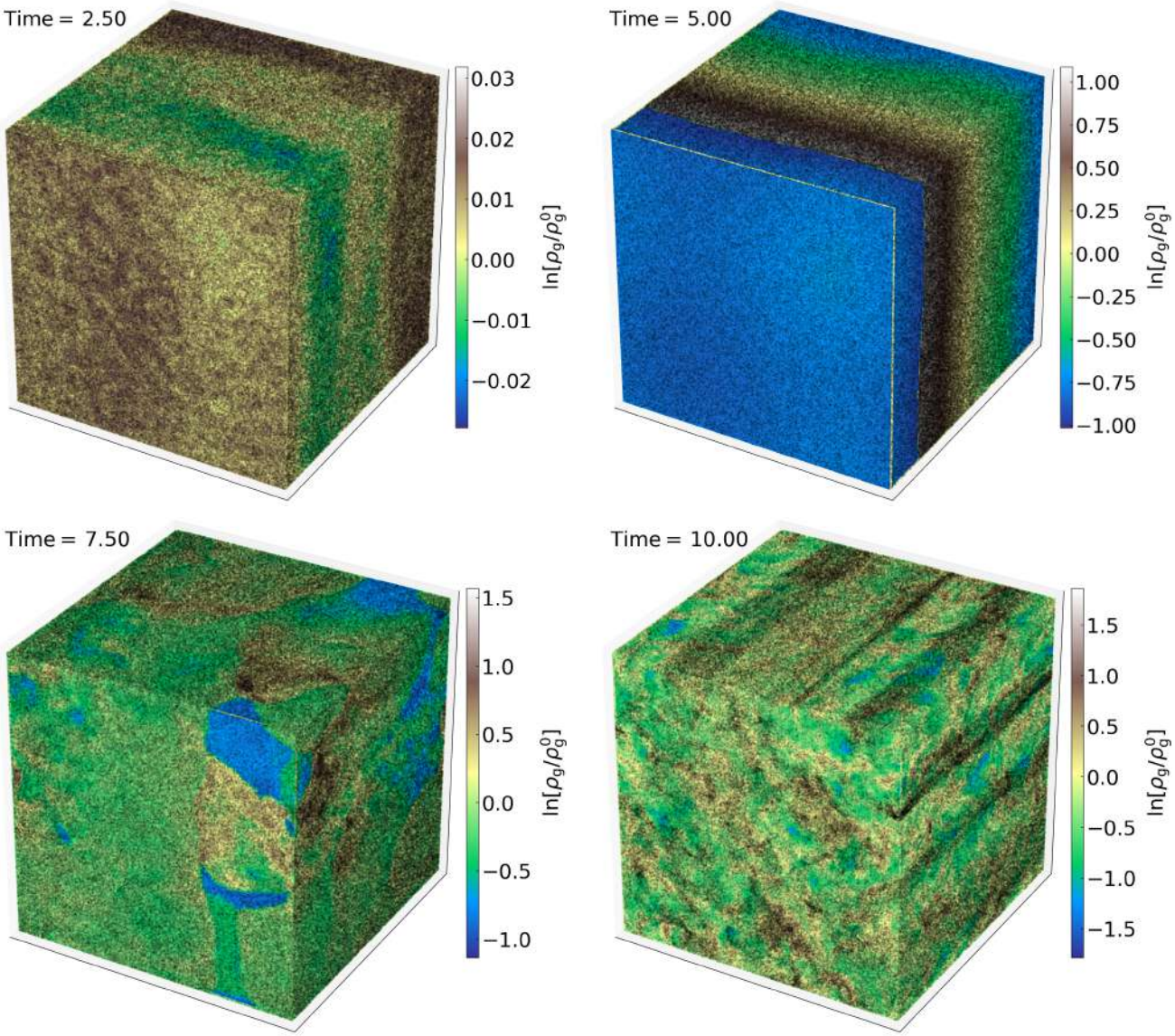

Figure 1. Structure of the RDIs for the simulation *RDI-const* where we assume that all dust particles feel the same acceleration regardless of their size. We show four different points in time, $t = 5$ (upper left), $t = 10$ (upper right), $t = 15$ (bottom left) and $t = 20$ (bottom right). In this case the RDIs form up in sheets at early times but walk through a transition towards elongated cylinders for later times.

4.3 Optical depth

In this section we want to evaluate the influence of the RDIs on the geometrical optical depth. We already pointed out in section 3 that the geometrical optical depth is by constraints of the initial conditions a fixed property of the simulation that only depends on the initial grain sizes and the underlying grain-size-distribution. However, even if the geometrical optical depth is a quantity that is fixed over the whole box it is still intuitively clear that the build up of the RDIs in the system can have a huge impact on the local properties of the geometrical optical depth. This is due to the simple fact that the geometrical optical depth is mainly dependent on the total number of dust particles along a certain line of sight. Because the RDIs lead to an overpopulation (or under population respectively) of dust particles in certain regions of the box the geometrical optical depth can increase (or decrease) significantly. This is even more crucial if the certain region contains a lot of dust particles that follow the lower end of the grain size distribution as we pointed out in section 3 as the lower end dominates the behavior of the geometrical optical depth.

There are several methods to calculate the geometrical optical depth along the line of sight. We test two different methods here. In the first method we calculate the geometrical optical depth by summing up particles in a specific cylinder with a specific radius. This large cylinder can be subdivided in smaller cylinders. For each cylinder we calculate the the geometrical optical depth by summing up over the grain sizes within this cylinder. The procedure is presented in figure 6. Now, we have two options to calculate the geometrical optical depth within the cylinders. The most simple one is by calculating the geometrical optical depth of the large cylinder by building the mean value of the geometrical optical depths of the smaller cylinders which leads to

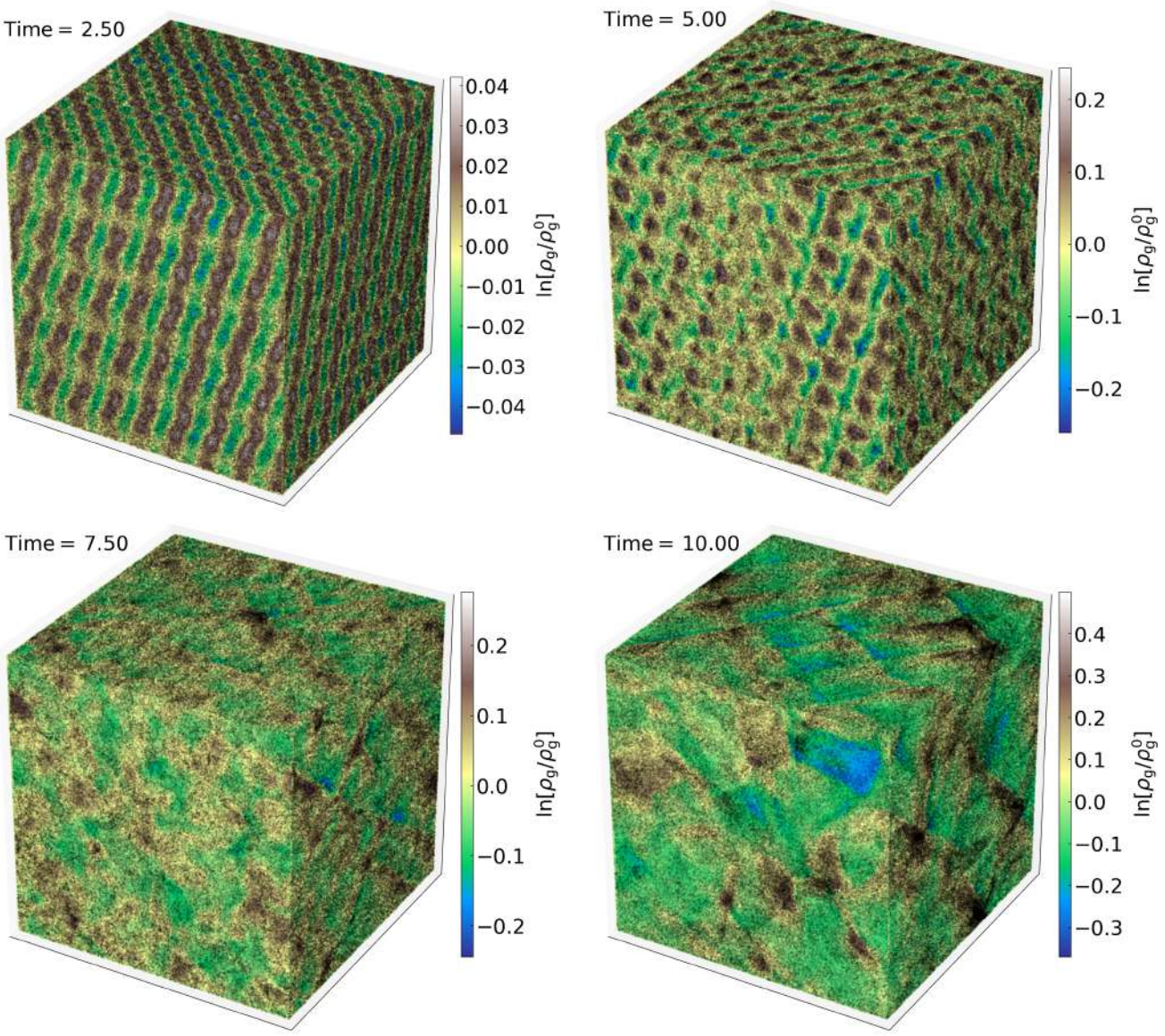

Figure 2. Same as figure 1. In this case the RDIs form more rapidly and more randomly compared to the behaviour we could observe in 1.

$$\tau_{\mathrm{large}} = \frac{1}{N}\sum_{i}^{N} \tau_{\mathrm{small}}^{i}, \tag{20}$$

with τ_{large} as the geometrical depth of the large cylinder, N as the number of small cylinders and $\tau_{\mathrm{small}}^{i}$ as the individual geometrical optical depth of the cylinder with the index i. Although, this method performs very well in most cases, there is a more accurate way to calculate the geometrical optical depth of the big cylinder from the optical depths of the small cylinders. This is by calculating the optical depth from the average of the covering fraction f_{c} which is given by

$$f_{\mathrm{c}} = \frac{1}{N}\sum_{i} \exp -{\tau_{\mathrm{c}}}^{i}. \tag{21}$$

We can then calculate the geometrical optical depth of the large cylinder by evaluating the expression

$$\tilde{\tau} = -\ln f_{\mathrm{c}}. \tag{22}$$

However, this approach is quite accurate but also computational quite expensive due to the high particle numbers that we have in the simulation. Therefore we present a second, more efficient way to calculate the geometrical optical depth of a single large cylinder for a given point in time. The trick is to tabulate the geometrical optical depth for the small cylinders on a rectangular grid . This means that the small cylinders actually become small rectangular cuboids. We note that this does not change the methodology described above but reduces the computational effort by a significant amount. The procedure is illustrated in figure **??**. For the size of the grid we choose 256x256 pixels. This is given by the resolution of our simulations. Given our resolution of $4 \cdot 256^3$ dust particles, we have (on average) 1000 dust particles in one bin which we assume a reasonable number. It is small enough to not get the box average of the optical depth but large enough to not be dominated

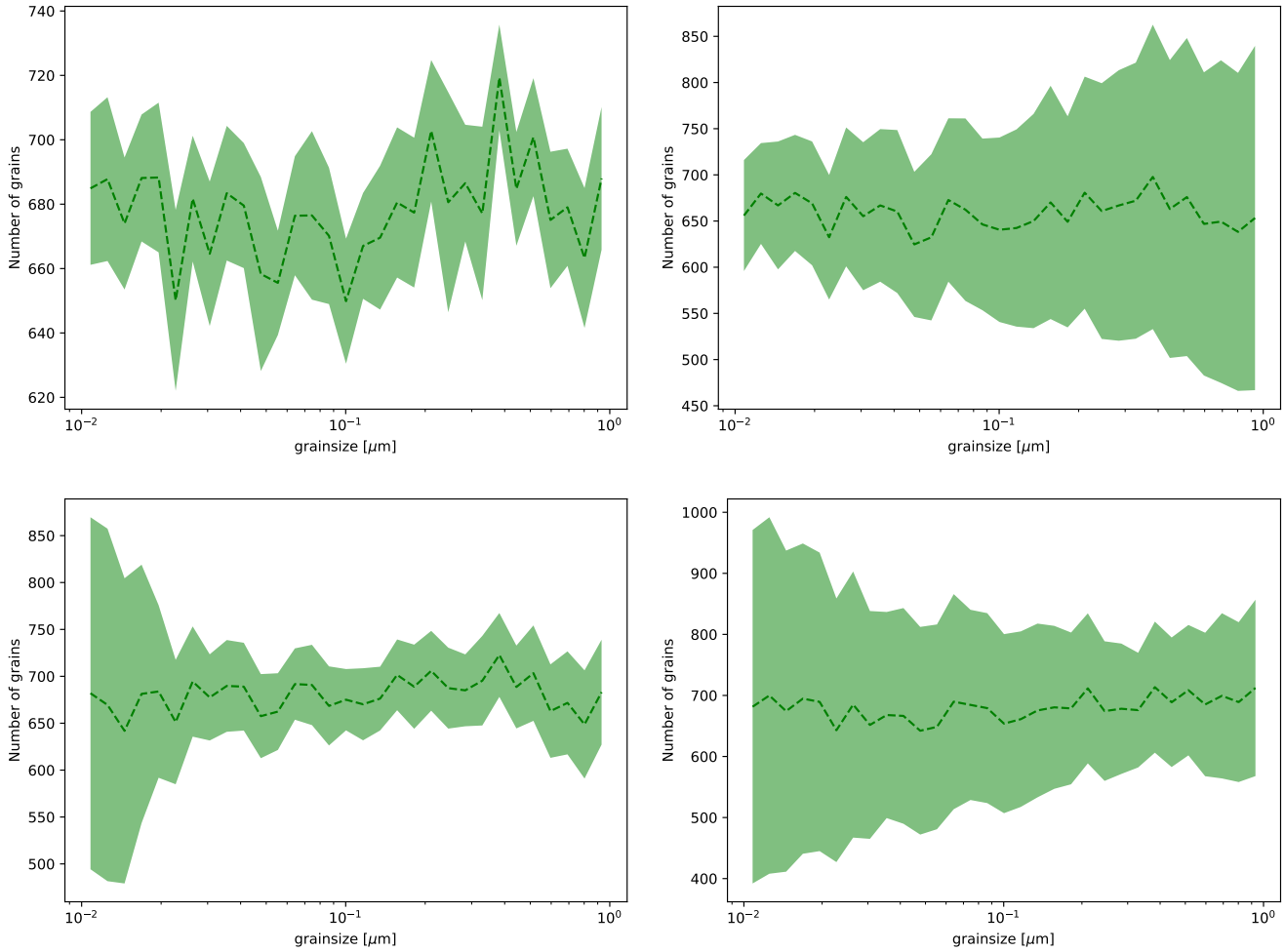

Figure 3. Mean value (dashed) and its scatter (shaded region) of the histograms of the grain sizes of 100 random line of sights through the whole box for the model *RDI-const* (top) and *RDI-noconst* (bottom). The two panels on the left represent $t = 5$ while the two panels on the right show $t = 15$. While the mean value of the grain sizes seems to be a constant with time the scatter behaves completely different between the two models. In the model *RDI-const* the RDIs are domianted by the large grains while the model *RDI-noconst* indicates the opposite.

by shot noise. We then draw a cylinder of a certain size around the grid points and make sure that we capture enough grid points to have enough values of $\tau_{\rm small}$ in each cylinder to calculate the geometrical optical depth in each large cylinder by an appropriate set of data points. We show our results in figure 7 in the case that the line of sight is alongside the xz-direction for the simulation RDI-noconst. In figure 8 we show the results from the optical depth calculations if the line of sight is alongside the xy-direction. We note that we do not have to consider the third line of sight along the yz-direction because it is statistically identical to the xz-direction. In both figures we show the same quantities from top to bottom. The top panel shows the time evolution of the geometrical optical depth for cylinders with four different radii which are centered around the midpoint of the box. We calculated the optical depth in this case with both methods the we presented in the beginning of the chapter and note that the differences are insignificant. Therefore, we decide to present the optical depth based on the second method in which we pre-calculated the optical depths in rectangular cylinders using a mesh with 256x256 grid points. Along both line of sights there is initially no change in the optical depth. We can understand this by keeping in mind that the RDIs need a certain formation time before they build up. This is in order of the stopping time of the system. Further, we can see that the smaller the cylinder is the larger are the jumps in the geometrical optical depths once the RDIs dominate the system. This can be understood by the fact that the RDIs can keep a large amount of dust particles in a relatively small spatial region. However, for larger radii it is straight forward to see that the optical depth is not fluctuating very strong as function around the initial value of the optical depht of the box. We futher notice that the fluctuations in the optical depth are stronger along the xy-direction due to the fact that this is the line of sightin which the instabilites build up. In the middle panel of the figures 7 and 8 we show the mean value of the geometrical optical depth as a function of time. In this case we draw 100 random cylinders in the box and calculate the optical depth via method two. Finally, we calculate the mean value of the optical depth over the covering fraction by applying equation 21 and 22. In both cases the mean value of the geometrical optical depth increases once the RDIs build up and fluctuates very strongly as a function of time. Once again for smaller cylinders we see more fluctuations about the initial value of the optical depth in the box. While in the xz-direction the mean value of the optical depth increases we observe a decrease of the mean value of the optical depth

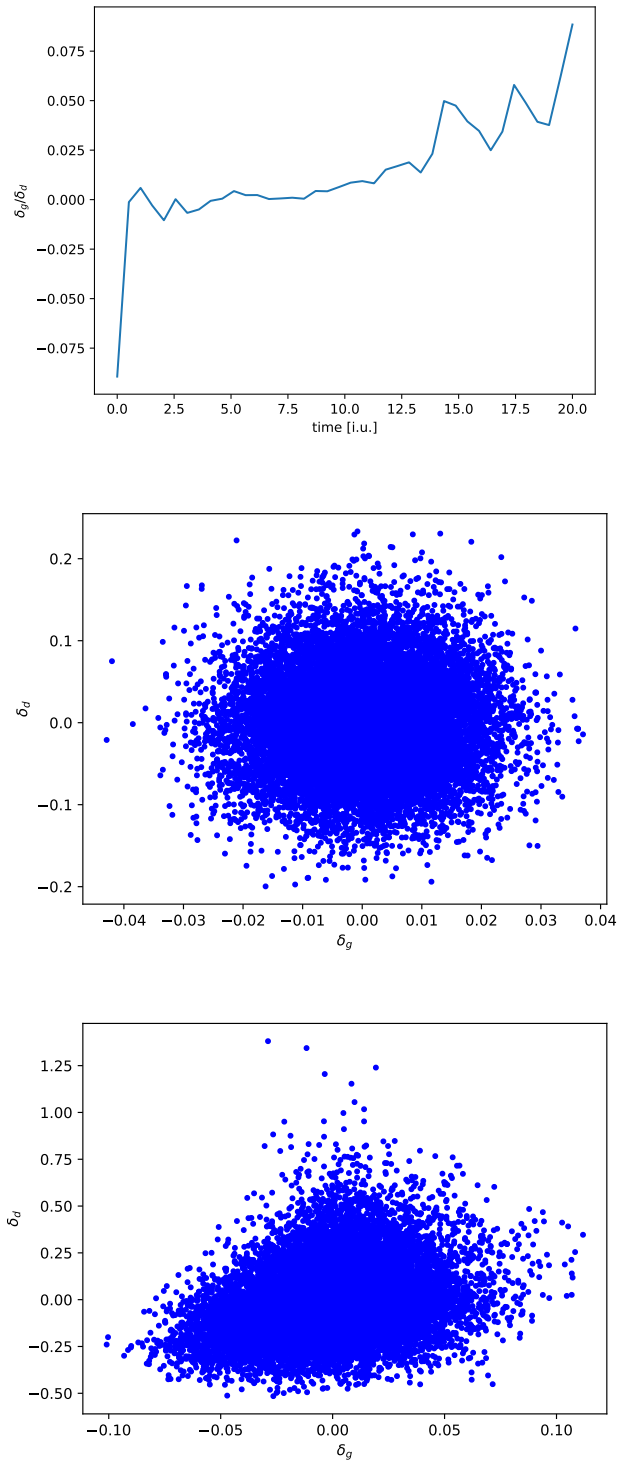

Figure 4. Time evolution of the median value of the bias (upper panel) between the gas and the dust particles in our simulation. The median value of the bias rises towards later times, leading to the conclusion that the dust and the gas become more correlated when the instabilities built up. This becomes clear when we look at the two bottom panels which show δ_{dust} as a function of δ_{gas} for $t = 5$ (middle) and ($t = 15$) before and after the RDIs arise.

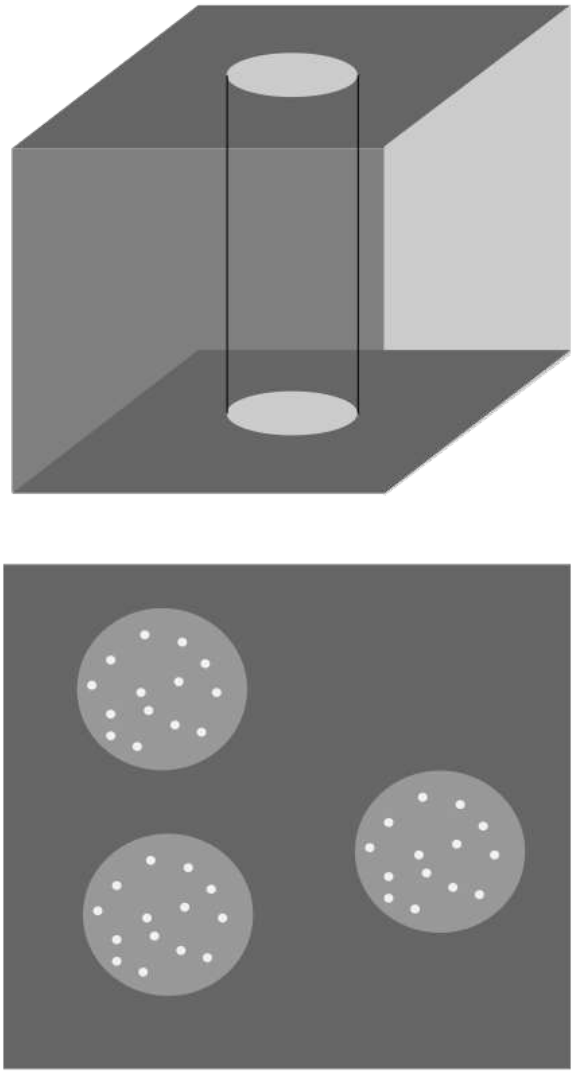

Figure 5. Illustration of the procedure to calculate the geometrical optical depth. A specific cylinder along a specific line of sight is chosen and subdivided in smaller cylinders. It is valid that these small cylinders contain not to much particles to actually capture the optical properties of the RDIs itself. If the cylinders are to large the geometrical optical depth will not differ from the overall optical depth within the box. However, empty cylinders are allowed, representing an optical depth of zero which can be of course the case for some cylinders due to the build up of the RDIs.

in the xy-direction. Finally, in the bottom panel of both figures we plot the standard deviation of the optical depth as function of time. We see that the standard deviation saturates in both cases saturates at around 0.1.

5 APPLICATIONS TO PHYSICAL SYSTEMS

5.1 Constraints given by the framework of an AGB star

One possible application to study the optical properties of the RDIs in greater detail in a physical system is a AGB star. In this chapter we discuss how we can constrain the physical system of an AGB-star. As already discussed in chapter ?? the whole simulation is characterized by three physical parameters, the dust-to-gas-ratio μ, the drift velocity of the dust (i.e. the external acceleration on the

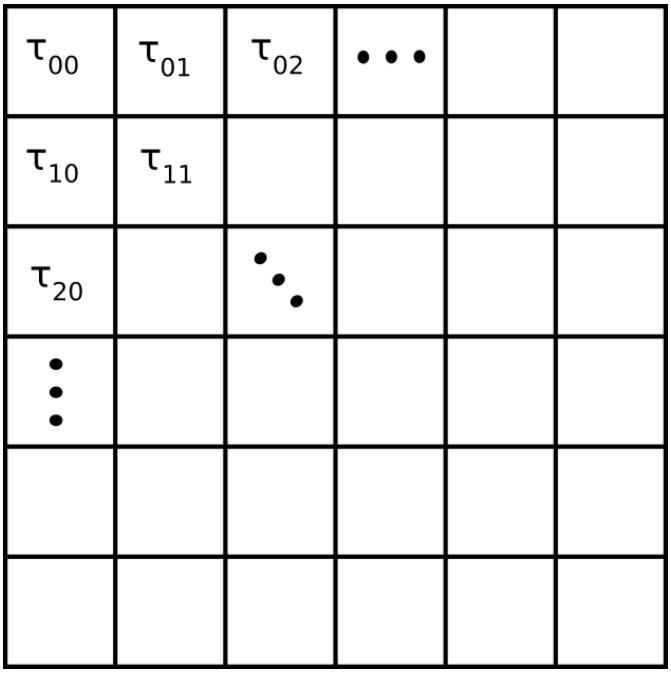

Figure 6. Illustration of the binning process. The values for each cell of the grid are obtained by summing up over all dust particles in the cell. The resolution of the underlying mesh is 256x256. The circle indicates the cylinder for which we want to calculate the optical depth. We get the optical depth of the cylinder by evaluating equations 21 and 22 for all the values of $\tau^i_{\rm small}$ in the large cylinder.

Table 1. Typical physical AGB-star parameter

Typical values for AGB stars from Observations	
Stellar mass $[M_\odot]$	0.6 – 10
Stellar radius $[R_\odot]$	10 – 250
Effective temperature [K]	2000 – 3000
Luminosity $[L_\odot]$	10^3 - 10^4
Wind velocity [km/s]	5 – 30
Mass loss rate $[M_\odot/yr]$	10^{-8} – 10^{-4}
Dust-to-gas ratio μ	$10^{-4} - 6 \cdot 10^{-3}$
Optical depth τ	0.5 – 1.2

dust particles) and the grain-size-parameter. However, the grain size-parameter is not a full physical parameter and is numerically given through equation refeq:grainsize. To constrain the system of an AGB-star properly we therefore need to come up with the correct dust-to-gas-ratio around this objects, an estimate for the acceleration parameter that is given by a typical AGB-star and a value for the minimum and maximum size for the grain size parameter. Typically, the wind of an AGB-star is defined by its luminosity $L_{\rm AGB}$, its mass loss rate $\dot{M}_{\rm AGB}$ and the velocity $v_{\rm AGB}$. Moreover, the size of the AGB-star $R_{\rm AGB}$ is an important quantity to define the system. Further, we need to assume a typical value for the optical depth $\tau_{\rm AGB}$ in the close neighborhood of the system. We show typical values for this parameters in table 1 and discuss them briefly in the following section.

Stars on the AGB-branch are stars which are in the stage of burning helium to carbon in the so called triple-α process. In this

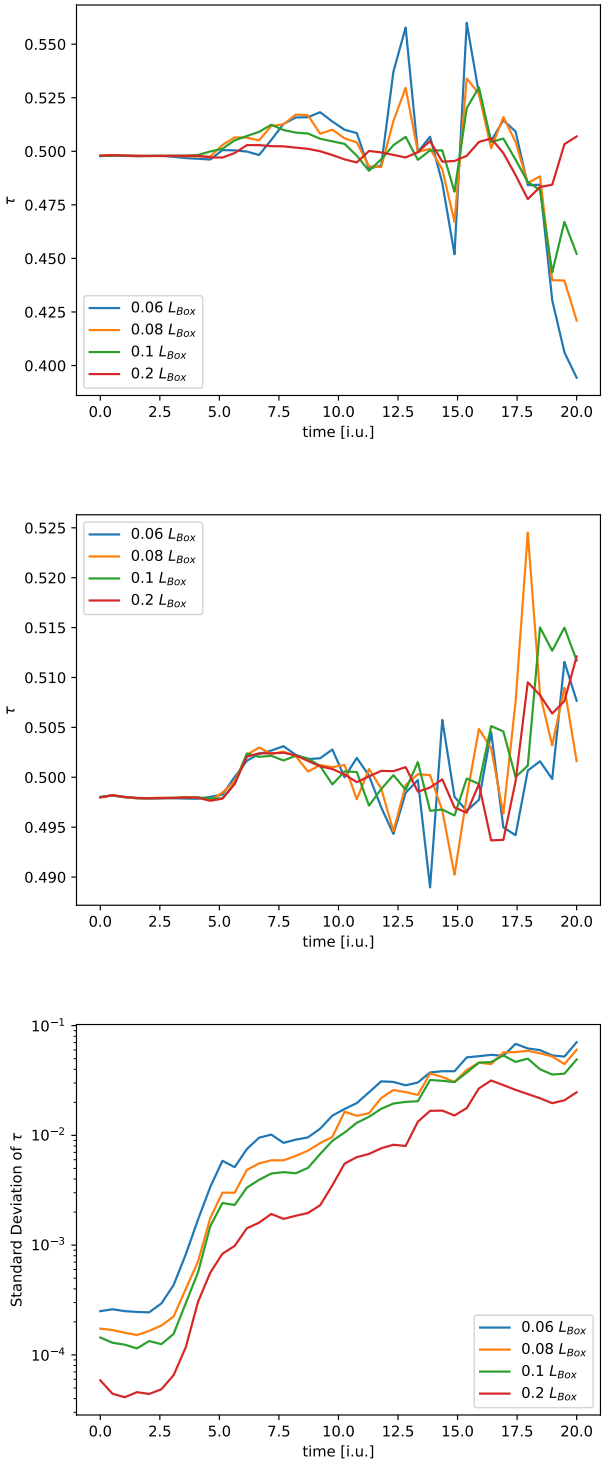

Figure 7. Mean value of the optical depth τ (upper panel) averaged over 100 randomly drawn cylinders for each point in time. The mean value of τ is investigated for six different cylinder radii which are scaled in terms of the box size from $0.04L_{Box}$ to $0.4L_{Box}$. In the beginning of the simulation the average value is close to the overall optical depth within the Box. For later times when the RDIs become important the mean value of the optical depth starts to fluctuate. The bottom panel shows the standard deviation of the values τ. In the beginning when the instabilities have not build up yet. The fluctuations of the optical depth are small. For later times the standard deviation of the optical depth τ grows, indicting indirectly the build up of the instabilities.

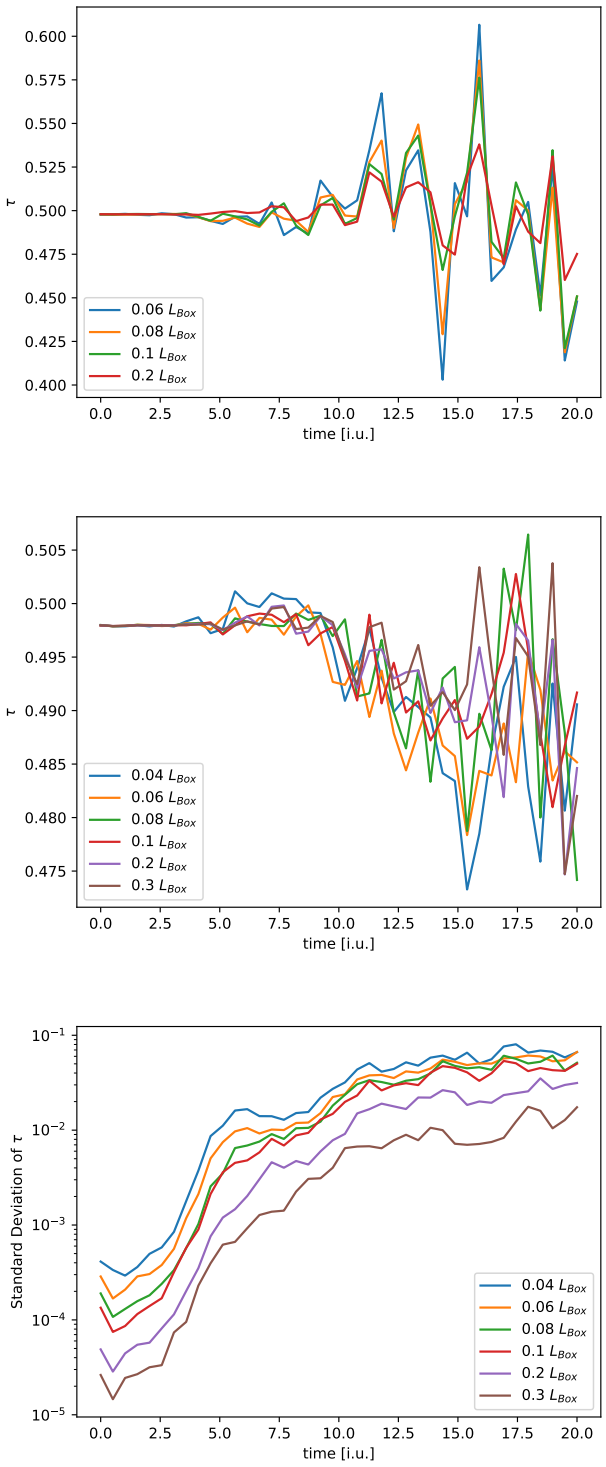

Figure 8. Mean value of the optical depth τ (upper panel) averaged over 100 randomly drawn cylinders for each point in time. The mean value of τ is investigated for six different cylinder radii which are scaled in terms of the box size from $0.04 L_{\rm Box}$ to $0.4 L_{Box}$. In the beginning of the simulation the average value is close to the overall optical depth within the Box. For later times when the RDIs become important the mean value of the optical depth starts to fluctuate. The bottom panel shows the standard deviation of the values τ. In the beginning when the instabilities have not build up yet. The fluctuations of the optical depth are small. For later times the standard deviation of the optical depth τ grows, indicting indirectly the build up of the instabilities.

process, three helium-cores fuse to one single carbon core and put out an energy of around 25 MeV. While the stars are on the AGB-branch they are in hydro static equilibrium. Although, the stars are stable once they reach the AGB-branch there are requirements on the initial mass for the stars to populate the AGB-branch. The lower limit is to be roughly $0.6 M_{\odot}$ dominated by the fact that the star must be heavy enough to survive the Helium-flash, when the core abruptly expands due to the transition from a degenerate equation of state to a adiabatic equation of state. The lower limit is set to around $10 M_{\odot}$ by the fact that stars with a higher mass never reach hydro static equilibrium via the triple-α-process. While moving towards the AGB-branch the stars increase in size due to the fact that the core collapses and heats the caveat from below leading to enhanced hydrogen burning in the envelope and a larger radius. The objects can reach radii up to 1 $Au (\propto 250 R_{\odot})$. The increase of the radius leads to a drop of the effective temperature to a value of between 2000 and 3000 K. However the effective temperature and the radius of the star determine its luminosity, given by $L/L_{\odot} = (R/R_{\odot})^2 (T/T_{\odot})^4$. While the effective temperature drops but stays inside the same order off magnitude but the radius can easily increase by a factor of 100 the typical luminosity's can reach values up to $10^4 L_{\odot}$. While most values of AGB-stars are quite extreme compared to stars on the main sequence, the wind velocities of these objects are quite low compared to solar-like main-sequence stars and reach maximum values between 5 and 30 km/s. These winds are driven by dust in the lower atmosphere of the star, triggered by high mass loss rates of AGB-stars between 10^{-8} and $10^{-4} M_{\odot}/yr$, leading to values of μ in the neighborhood of the star between 10^{-4} and $6 \cdot 10^{-3}$. The optical depths are between 0.5 and 1.2. This parameter space can be used to constrain the ICs for a box that represents a patch of an AGB-star wind in the close neighborhood (a few $R_{\star}$) of the star. We carry that out in three steps, by assuming reasonable values for the AGB star.

- Choose a set of parameters by selecting a certain optical depth for the box.
- Calculate the grain-size-parameter in code units for a given optical depth of the box.
- Use the grain-size-distribution to calculate the acceleration parameter in code units for a given Luminosity of the star.

We note that we do not want the system to be to extreme in either direction and therefore we assume intermediate values for all parameters.

5.1.1 *Constraints for the optical depth*

We want choose the optical depth to be 1 within the simulation. The optical depth of the Box depends on a few parameters, especially the dust-to-gas-ratio μ, the distance from the stars surface and the mass loss rate of the star. We can approximate the optical depth by calculating

$$\tau = \frac{\mu}{0.01} \frac{R}{1000 R_{\odot}} \frac{\dot{M}}{10^{-6}} \tag{23}$$

If we choose not to extreme values for the dust-to-gas we can obtain a reasonable value for the optical depth. We choose the dust-to-gas ratio to be $\mu = 0.001$, the distance from the star to $1000 R_{\odot}$ and an intermediate outflow rate of $M_{\odot}$ of $10^{-6} M_{\odot}/yr$. This gives an optical depth of 0.1. While this value seems to be to low if we apply single grain sizes it fits very well if we apply the more physical case of a grain size distribution given by equation 4, as the optical

depth is dominated by the grains with smaller size. This is pointed out in section 3. In the case of this grain size distribution we get a value of the optical depth which is exactly a factor of 10 larger. Therefore, this set of parameters defines a box with an optical depth of 1.0.

5.1.2 Calculating the grain size parameter α

Under the assumption of the optical depth that we calculated in section 5.1.1 we can derive the value for the grain-size-parameter α. We already derived the dependence between the grain size parameter α and the optical depth in equation 10 in the case of constant grain sizes. We note that we need just to calculate the maximum grain size. If we set the minimum of the grain size parameter to 1 percent of the maximum grain size we will automatically obtain an optical depth of 1.0. We can therefore calculate the maximum grain size parameter with the relation

$$\alpha_{\mathrm{max}} = \frac{3}{4}\frac{\mu}{\tau} \tag{24}$$

This sets the numerical value for α_{max} to 0.0075. The minimum for the grain size parameter is therefore set to 0.000075. This parameters are chosen to obey the physical system of an AGB-star system in the unit-system we use for running the simulations.

5.1.3 Calculating the acceleration parameter

Finally, we can calculate the acceleration parameter by taking the grain size parameter into account. A lengthy calculation leads to the relation between the acceleration parameter a_{cc} in code units and the grain size parameter α given by

$$a_{\mathrm{cc}} = \frac{3}{4}\alpha\frac{10^3 L_{\odot}\dot{M}}{4\pi r^2}, \tag{25}$$

This leads to a acceleration parameter of around 2000 in code units.

5.1.4 The physical unit system

So far we set the parameters for the boxes in reduced units in a way that it is connected to the framework of an AGB star. However, the final step that is missing is to convert the unit less system into physical units. We adopt the units for the dust grains as follows. The maximum grain size a_{max} is set to $1\mu m$ which is in agreement with observations Draine & Salpeter (1979); Weingartner & Draine (2001). Using this definition we directly find the minimum grain size which is given by $a_{\mathrm{max}}/100$ given via the initial grain size distributions that has been used in the original setup. To calculate the particle masses of the dust grains we assume the mean density for the dust grains given by $\langle\rho_{\mathrm{d}}\rangle = 2$ g/cm^{-3} which is also in good agreement with the observations of dust particles in the ISM and protoplanetary discs. Further, we assume the dust particles to be spherical. Therefore, the mass m_{d} of the dust particles is given by

$$m_{\mathrm{d}} = \langle\rho_{\mathrm{d}}\rangle \cdot \frac{4}{3}\pi a_{\mathrm{d}}^3. \tag{26}$$

Using this definitions it becomes possible to define our system of units for the surrounding of a GMC as well as an AGB-star. We can calculate a physical box size by using equation 5 and specify the grain size density $\langle\rho_{\mathrm{g}}\rangle = 2g/cm^3$, the grain size $a_{\mathrm{g}} = 0.0001cm$, and the gas density $\langle\rho_{\mathrm{gas}}\rangle = \dot{M}/4\pi r^2 v_{\mathrm{w}}$. This leads to a box size of the physical system of $184R_{\odot}$. Using that we can derive the time unit over the wind speed of roughly $10km/s$ to 0.40 years.

ACKNOWLEDGMENTS

UPS acknowledges funding provided by the Kavli Foundation and the Simons Foundation as part of the Kavli Summer Program in Astrophysics 2018. UPS acknowledges hostility provided by the Center of Computational Astrophysics in New York City who provided office space while this research project was carried out. UPS acknowledges support by an Emmy Noether grant of the Deutsche Forschungsgemeinschaft (DFG, German Research Foundation) under the project number MO 2979/1-1. The Flatiron Institute is supported by the Simons Foundation. Support for PFH was provided by an Alfred P. Sloan Research Fellowship, NSF Collaborative Research Grant 1715847 and CAREER grant 1455342, and NASA grants NNX15AT06G, JPL 1589742, 17-ATP17-0214. The authors acknowledge the computing time provided by the Caltech computing facilities on the cluster Wheeler as well as allocations from XSEDE TG-AST130039 and PRAC NSF.1713353 supported by the NSF, and NASA HEC SMD-16-7592.

REFERENCES

Bai X.-N., Stone J. M., 2010, ApJ, 722, 1437
Beck A. M., et al., 2016, MNRAS, 455, 2110
Carballido A., Stone J. M., Turner N. J., 2008, MNRAS, 386, 145
Draine B. T., Salpeter E. E., 1979, ApJ, 231, 77
Gaburov E., Nitadori K., 2011, MNRAS, 414, 129
Höfner S., Olofsson H., 2018, A&A Rev., 26, 1
Hopkins P. F., 2015, MNRAS, 450, 53
Hopkins P. F., Squire J., 2017, preprint, (arXiv:1707.02997)
Hopkins P. F., Squire J., 2018, MNRAS,
Hu C.-Y., Naab T., Walch S., Moster B. P., Oser L., 2014, MNRAS, 443, 1173
Johansen A., Youdin A., Mac Low M.-M., 2009, ApJ, 704, L75
Kaiser N., 1984, ApJ, 284, L9
Mathis J. S., Rumpl W., Nordsieck K. H., 1977, ApJ, 217, 425
Pan L., Padoan P., Scalo J., Kritsuk A. G., Norman M. L., 2011, ApJ, 740, 6
Springel V., 2010, MNRAS, 401, 791
Squire J., Hopkins P. F., 2018a, MNRAS, 477, 5011
Squire J., Hopkins P. F., 2018b, ApJ, 856, L15
Weingartner J. C., Draine B. T., 2001, ApJ, 548, 296

This paper has been typeset from a TEX/LATEX file prepared by the author.